

RESEARCH ARTICLE

10.1002/2016JA022666

Key Points:

- Interplanetary shock-generated auroral streaks moved antisunward along the poleward boundary of the dawnside oval
- The streak moving speed in the ionosphere is consistent with the speed of surface waves on the dawnside magnetopause
- The auroral streaks can be caused by postaccelerated electrons by a field-aligned potential drop inside sheared flux tubes

Supporting Information:

- Supporting Information S1

Correspondence to:

X.-Y. Zhou,
xyzhou@igpp.ucla.edu

Citation:

Zhou, X.-Y., G. Haerendel, J. I. Moen, E. Trondsen, L. Clausen, R. J. Strangeway, B. Lybekk, and D. A. Lorentzen (2017), Shock aurora: Field-aligned discrete structures moving along the dawnside oval, *J. Geophys. Res. Space Physics*, 122, 3145–3162, doi:10.1002/2016JA022666.

Received 4 MAR 2016

Accepted 7 FEB 2017

Accepted article online 13 FEB 2017

Published online 15 MAR 2017

Shock aurora: Field-aligned discrete structures moving along the dawnside oval

Xiaoyan Zhou^{1,2} , Gerhard Haerendel³ , Jøran I. Moen⁴, Espen Trondsen⁴, Lasse Clausen⁴ , Robert J. Strangeway¹ , Bjørn Lybekk⁴, and Dag A. Lorentzen⁵ 

¹Department of Earth and Space Sciences, University of California, Los Angeles, California, USA, ²XYZ Space Physics, Inc., Pasadena, California, USA, ³Max Planck Institute for Extraterrestrial Physics, Garching, Germany, ⁴Department of Physics, University of Oslo, Oslo, Norway, ⁵University Centre in Svalbard, Svalbard, Norway

Abstract Generated by interplanetary shocks or solar wind pressure pulses, shock aurora has transient, global, and dynamic significances and provides a direct manifestation of the solar wind-magnetosphere-ionosphere interaction. As a part of a series of studies of the shock aurora, this paper focuses on the interaction at the morning magnetopause and its auroral manifestation at ~06 magnetic local time, where the velocity and magnetic field shears dominate the interaction. Flow shears can generate wave-like structures inside a viscous boundary layer or even larger-scale vortices. These structures couple to the ionosphere via quasi-static field-aligned currents or via kinetic Alfvén waves. Potential drops along field-aligned filaments may be generated accelerating electrons to form auroral manifestations of the structures. A shock aurora event at dawnside is used to test this scenario. The findings include moving auroral streaks/rays that have a vertical profile from red (at ~250 km altitude) to purple (at ~100 km). The streaks moved antisunward along the poleward boundary of the oval at an ionospheric speed of ~3 km s⁻¹. It was mapped to the magnetopause flank at ~133 km s⁻¹, which was consistent with the observed speed of the magnetopause surface waves generated by the Kelvin-Helmholtz instability. The calculated field-aligned potential drop using Haerendel's analytic model was ~5 kV that reasonably explained the observations. The results support the above scenario and reveal that magnetic and velocity shears at the flanks of the magnetopause may be the main cause of the fast moving shock aurora streaks.

1. Introduction

As the term suggests, shock aurora is the auroral activity caused by interplanetary shocks (or solar wind pressure pulses that have a dynamic pressure jump as forward shocks do). The aurora, as a direct manifestation of the solar wind-magnetosphere-ionosphere coupling, has a transient, global, and dynamic significance and provides an opportunity to derive the remote magnetospheric and solar wind processes from the auroral forms and their variations based on the precise timing between the cause and effect. Such auroral signatures were first recorded by the DE 1 satellite when the entire auroral oval was lit up after an interplanetary shock [Craven *et al.*, 1986]. With enhanced technology capability and scientific interests, details of the auroral process and corresponding mechanisms were revealed gradually. The auroral remote sensing from the Polar UVI provided auroral images at a cadence of ~36 s [Torr *et al.*, 1995] and showed the shock aurora onset at or near local noon and then propagating to the nightside along the oval [Spann *et al.*, 1998; Zhou and Tsurutani, 1999; Vorobjev *et al.*, 2001] at a speed of ~6–11 km s⁻¹ in the ionosphere. This scenario was later confirmed by in situ observations from FAST and DMSP satellites [Zhou *et al.*, 2003], ground-based ASI (all-sky imager) observations [Zhou *et al.*, 2009; Holmes *et al.*, 2014], and GPS total electron content intensifications [Jin *et al.*, 2016], which further revealed that the discrete shock aurora is located at high latitudes along the boundary between open and closed field lines and that the diffuse shock aurora is mainly below that boundary at closed field lines. The fast moving aurora is the diffuse shock aurora.

As described by Zhou and Tsurutani [1999], the most pronounced compression effect appears in the dayside sector centered on the shock impact location where the magnetopause is displaced the most by the compression. It even can expose the geosynchronous orbit to the solar wind when a shock or pressure pulse is very intense. The compression initiates wave instabilities and wave-particle interactions at lower L shells and, in turn, leads to auroral emissions at lower magnetic latitudes (MLAT), such as local noon subaurora patches to occur at 60° MLAT as reported by Liou *et al.* [2002], Meurant *et al.* [2004], and Jin *et al.* [2016]. In

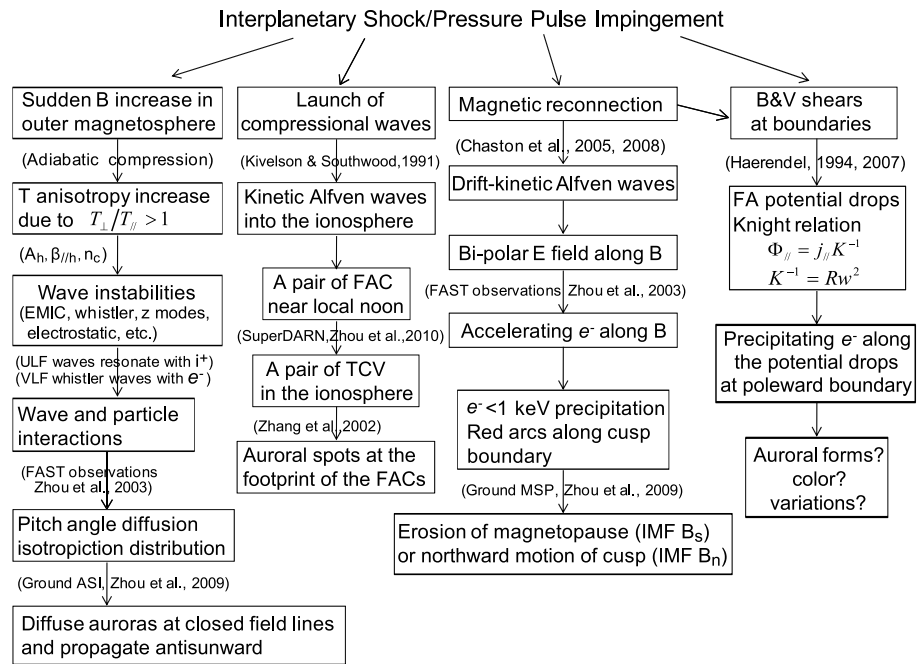


Figure 1. Tracing the interplanetary shock/pressure pulse compression from the magnetopause to the auroral ionosphere.

addition to the physical displacement of the magnetopause, the coupling of the compressional waves to kinetic Alfvén waves suggests the formation of a pair of field-aligned currents (FACs) and corresponding ionospheric vortices around local noon [Tamao, 1964; Araki, 1994; Kivelson and Southwood, 1991; Vorobjev et al., 2001; Zhou et al., 2010]. This can explain the spots of proton aurora around local noon as caused by pressure pulses and shocks [Zhang et al., 2002, 2004; Frey et al., 2002, 2003; Hubert et al., 2003; Meurant et al., 2004] with the coexisting electromagnetic ion cyclotron (EMIC) waves with FACs causing the proton precipitation [Fuselier et al., 2004; Zhang et al., 2008].

The detection of proton aurora is owed to one of the IMAGE FUV spectrographic imaging instruments, SI-12 [Mende et al., 2000]. Proton shock aurora provides an additional approach to monitor plasma drift and wave activity under various solar wind and interplanetary magnetic field (IMF) conditions. Similar to the electron shock aurora, the proton aurora first occurs around local noon then propagates antisunward along the oval at very high ionospheric speed. However, the proton aurora is more pronounced at the duskside, especially when the IMF is southward upstream of the shock indicating an enhanced azimuthal drift of newly injected plasma [Meurant et al., 2003, 2004; Laundal and Østgaard, 2008].

Those previous studies have shown that interplanetary shocks and pressure pulses trigger sudden and, most of the time, significant changes in the geospace system. Therefore, there is less ambiguity when tracing an ionospheric disturbance back to the cause and the driver in the magnetosphere, which can be tens of Earth's radii away where it can hardly be captured by in situ observations. This advantage becomes evident in the comprehensive diagram in Figure 1 that maps the compressional effects from magnetopause and outer magnetosphere to the auroral forms in the ionosphere. The left column traces the adiabatic compression from the outer equatorial magnetosphere to the auroral ionosphere. One prominent compression effect is the sudden increase of the magnetic field intensity in the dayside outer magnetosphere when a shock pushes the magnetopause earthward. Compared to the electron gyroperiod of milliseconds, the dayside compression at a time scale of seconds to minutes can be treated as adiabatic. This adiabatic compression leads to an enhancement of the temperature anisotropy and wave instabilities that result in wave-particle interactions and pitch angle scattering [e.g., Tsurutani et al., 1998, 2001]. Consequently, as the pitch angle scattering increases, the pancake-shaped distribution in the dayside magnetosphere becomes more isotropic sending more particles to the loss cone, which causes diffuse aurora. The diffuse auroras are seen from red to purple [Zhou et al., 2009; Holmes et al., 2014], indicating scattered electrons with energies from few hundred eV to tens of keV, although in situ observations by FAST show

that the isotropic electrons mainly have energies in the 1–20 keV range [Zhou *et al.*, 2003]. As the shock drives the adiabatic compression antisunward, the diffuse shock aurora is seen to propagate as well anti-sunward with the same angular speed as the shock in the solar wind. This has been confirmed by different observations [e.g., Zhou and Tsurutani, 1999; Holmes *et al.*, 2014; Jin *et al.*, 2016].

The second column from the left traces the effect of the compressional waves launched by the shock impingement at the subsolar magnetopause. This topic has a long history and caught a lot of attention. There have been observations and hypotheses that sudden changes in the solar wind dynamic pressure cause the ionospheric traveling convection vortex (TCV) [Friis-Christensen *et al.*, 1988; Sibeck *et al.*, 1989; Russell and Ginskey, 1995; Sibeck and Korotova, 1996]. Furthermore, the TCVs at near local noon are suspected to be the ionospheric manifestation of a pair of FACs generated during SCs (sudden commencements)/SIs (sudden impulses), i.e., by the shock impingement [e.g., Araki, 1994; Zhou *et al.*, 2010]. Theoretically, the FAC is carried by guided shear waves (presumably the Alfvén mode) that can be generated in the cold plasma when it is suddenly compressed [Tamao, 1964; Kivelson and Southwood, 1991]. On the basis of Super Dual Auroral Radar Network (SuperDARN) observations and ground-based magnetograms, Zhou *et al.* [2010] reported that a pair of TCVs occurred at ~11 magnetic local time (MLT) and 73° MLAT, and 13 MLT and 67° MLAT, respectively, within ~30 s after the shock arrival, although the lifetime was only 4–6 min. They speculated that the pair of FACs and TCVs might explain the spots of proton aurora generated by solar wind pressure pulses in the local noon sector [Zhang *et al.*, 2002; Hubert *et al.*, 2003]. This is because EMIC waves that coexist with FACs [Erlandson *et al.*, 1988; Erlandson and Zanetti, 1998] can interact with protons and cause the proton precipitation along the FACs. So one can expect to see proton aurora at the ionospheric footprint of the FACs [Fuselier *et al.*, 2004; Zhang *et al.*, 2008]. When approaching the ionosphere, protons experience multiple charge capture and charge loss processes while interacting with the neutral atmosphere. Depending on the penetrating proton's energy, these charge exchange processes can repeat hundreds or thousands of times, until the energetic protons end up as thermal protons in the lower atmosphere. After any charge capture process, the resulting neutral energetic hydrogen atom might emit light. Therefore, proton/hydrogen aurora has no structure and spreads in an area without sharp boundary, but containing the footprints of the FACs.

The third column from the left traces the dayside magnetopause reconnection down to the aurora. Magnetic reconnection is one of the fundamental and continuing interactions between the interplanetary magnetic field and the magnetosphere. However, the shock compression can significantly intensify this process. For example, the reconnection rate increases with increasing solar wind dynamic pressure because of the enhanced magnetosheath plasma density and magnetic field strength and of the inward flow into the reconnection diffusion region [e.g., Song and Lysak, 1994; Cassak and Shay, 2007]. Or the enhanced solar wind flow speed in the sheath will increase the fast mode Mach number that is one of the two primary controllers of the dayside merging rate [Lopez, 2016]. Based on Cluster observations on the dayside magnetopause, Chaston *et al.* [2005] confirmed that magnetic reconnection is the source of drift-kinetic Alfvén waves. The observed E_{\perp}/B_{\perp} is consistent with the homogeneous theory and a linear dispersion relation of drift-kinetic Alfvén waves. In addition, electrons modulated by the Alfvén waves are field aligned with energy lower than 1 keV. In the auroral acceleration region above the ionosphere such enhanced soft and field-aligned electron populations with the companion of broadband VLF waves are detected by FAST during shock aurora events [Zhou *et al.*, 2003]. Previous studies also showed that when the IMF is southward around the shock, auroral arcs along the cusp are lit up and followed by a meridional widening of the cusp toward south [Zhou *et al.*, 2009]. Such arcs are in red along the magnetic east-west direction while moving equatorward, indicating soft electron precipitations as a result of the low-latitude reconnection [Moen *et al.*, 1998; Sandholt *et al.*, 1998]. During northward IMF the reconnection occurs at the high-latitude magnetopause, which adds magnetic flux to the low latitude. So the aurora and cusp moves northward when the polar cap reduces its size [Oieroset *et al.*, 1997; Sandholt *et al.*, 1996].

The most right column in Figure 1 traces the magnetic and velocity shears on the magnetopause down to the ionosphere. This interaction is another fundamental and continuing process when the magnetic field in the magnetosheath moves along the magnetopause with the solar wind flow. Interplanetary shocks and pressure pulses enhance this interaction significantly because of the sudden increase in the velocity and magnetic field in the sheath. Magnetic shearing on flanks of the magnetopause has been reported during southward IMF [Paschmann *et al.*, 1993; Phan and Paschmann, 1996]. Such magnetic shears may provide

sources of field-aligned currents on the inside of the magnetopause boundary layer transporting energy and momentum toward the ionosphere. It is quite possible that the magnetic shear stresses are being converted into kinetic energy via field-aligned potential drops [Haerendel, 1994, 2007] accelerating auroral particles generating auroral emissions. While having been used to explain the poleward auroral arcs during a substorm [Haerendel, 2009] and structured arcs embedded in the convection along the evening auroral oval during a developed substorm [Haerendel, 2007], this analytical model has not been applied to the boundary between the solar wind and magnetosphere. Relevant auroral forms and their variations have not been studied and documented under this aspect. Therefore, there is an open question at the end of the right column in Figure 1.

Vortices can be generated on the magnetopause flanks during northward IMF conditions when the Kelvin-Helmholtz (KH) instability plays an important role [Otto and Fairfield, 2000; Fairfield et al., 2000]. The process has been theoretically studied by Miura [1992]. Hasegawa et al. [2004] studied, with the four Cluster spacecraft, the nonlinear vortices under northward IMF conditions even allowing the entry of solar wind plasma into the magnetosphere. Another consequence of a nonlinear KH waves may be the generation of sufficiently intense field-aligned currents so that parallel potential drops can develop and manifest themselves through accelerated electrons precipitating into the ionosphere. The corresponding auroral signature should be individual magnetic field-aligned structures, like streaks or rays, with an auroral spectrum covering all colors from red to green and to purple. The ionospheric footprints of the flux tubes that extend to the primary structures on the magnetopause LLBL (low-latitude boundary layer) should not be stationary but should, instead, move antisunward with a speed consistent with nonlinear propagating waves. Such a scenario combines the KH instability and vortices/nonlinear structures at the flank LLBL with the auroral acceleration process to explain dynamic auroral streaks/rays under shock conditions.

This paper addresses this scenario by analyzing a shock event during which auroral imaging observations from the ground were obtained at a location in the morning sector which maps to the dawnside outer magnetosphere and magnetopause. We are taking advantage of the shock condition to secure a convincing spatial and temporal agreement between data from the ionosphere, the LLBL magnetopause, and the solar wind. Observations from the all-sky imager (ASI) and meridian-scanning photometer (MSP) from Longyearbyen (LYR) on Svalbard were obtained at ~0630 MLT when the IMF B_z was near zero and northward. ASI images showed that shock intensified auroral streaks/rays moved westward away from the Sun with an ionospheric speed that matched the speed of the surface waves generated on the magnetopause flank by the KH instability. In addition, these streaks/rays were observed not only in the green line but also in the red, suggesting that the precipitated electrons may have an extended energy spectrum. These findings very well support the aforementioned scenario and address the questions in Figure 1, the fourth column from the left. We also discuss the mechanisms of the electron acceleration that caused the auroral streaks/rays.

2. Solar Wind Observations of the Interplanetary Shock

Figure 2 shows the solar wind data and geomagnetic indices $SYM-H$, AU , and AL from 0000 to 0600 UT on 18 February 1999. The 1 min solar wind data were from the OMNI website (<http://cdaweb.gsfc.nasa.gov/cgi-bin/eval2.cgi>), which have been shifted to the bow shock subsolar point. The vertical line at 0245 UT shows the shock front where the interplanetary magnetic field increased from ~7 to 12 nT, the IMF B_y remained positive from ~5 to 7 nT and the IMF B_z turned northward from ~0 to 4 nT. There was a substantial solar wind velocity increase from ~400 to 600 km s⁻¹ at the shock. The plasma density increased from ~2 to 8 cm⁻³. Consequently, the solar wind dynamic pressure increased from ~1 to 6 nPa. Note that the solar wind was quiet for several hours upstream of the shock during which IMF remained northward. The shock caused an increase in $SYM-H$ of ~30 nT, in AU of 35 nT, and a decrease in AL of ~10 nT.

3. Auroral Observations From the Ground

This shock caused a SI at ~0246 UT based on the NOAA/National Geophysical Data Center database (<http://www.ngdc.noaa.gov/stp/GEOMAG/geomag1.html>). There are data from ASI and MSP in LYR (75.2° MLAT) on Svalbard available for the interesting time interval. At the shock arrival Svalbard was

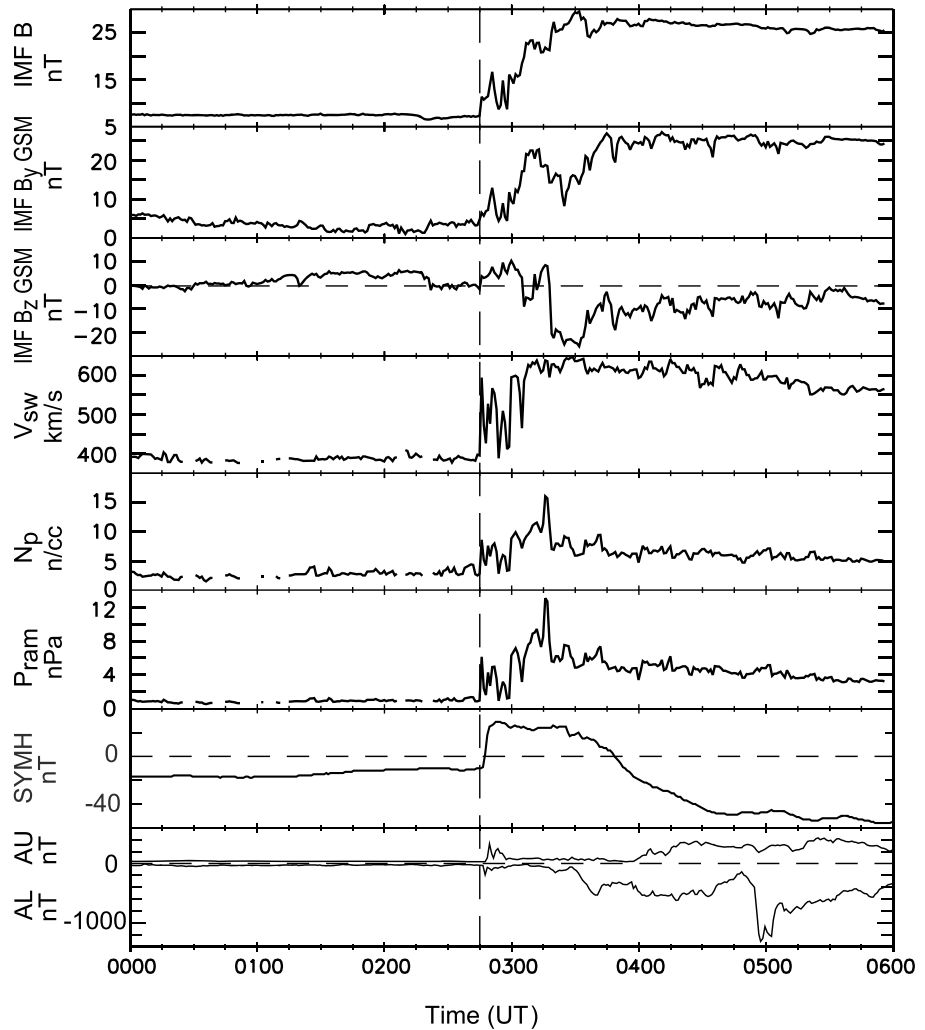


Figure 2. OMNI solar wind observations and geomagnetic indices in 0000–0600 UT on 18 February 1999. The solar wind data have been shifted to the subsolar bow shock. The shock is marked by the dashed line at ~0245 UT.

at ~0630 MLT. The ASI (operated by the University of Oslo, Norway) is an intensified silicon intensifier target camera system. It monitors 2-D auroral dynamics using a large field of view (FOV). Two filters are employed with one focusing at 557.7 nm (with 150° FOV) and the other at 630.0 nm (with 150° FOV). The auroral green (557.7 nm) and red (630.0 nm) line emissions correspond to transitions from $O(^1S)$ and $O(^1D)$ metastable states of oxygen, which have a radiative lifetime of ~1 s and ~110 s, respectively. In general, green-dominated emissions originate from ~120 km altitude, caused by hard electrons, and the red-dominated aurora originates from altitudes of ~250 km, caused by soft electrons with energy less than 1 keV.

In order to focus on the shock effect, we concentrate on auroral data in the first 30 min after the shock arrival from ~0245 to 0315 UT. Figure 3 shows auroral images in the green emissions, which have been projected into the MLT-MLAT coordinates. The red dashed curve in the first image at 0244:46 UT marks the poleward boundary of the auroral oval identified using FAST data (see the supporting information and discussions in section 4.1). One cannot simply conclude whether or not the aurora in the image above 78.5° MLAT was in the cap because of the distortion at large elevation angles and also due to the possible auroral overlapping along the line-of-sight direction. Therefore, we only discuss auroral features below the boundary. The black arrow between the second and third images of the top row marks the shock arrival at the subsolar magnetopause. There was a lack of evident changes in the aurora until 0247:45 UT when auroral streaks/rays in the northeastern sky and the diffuse aurora in the southern sky were intensified, indicating the shock

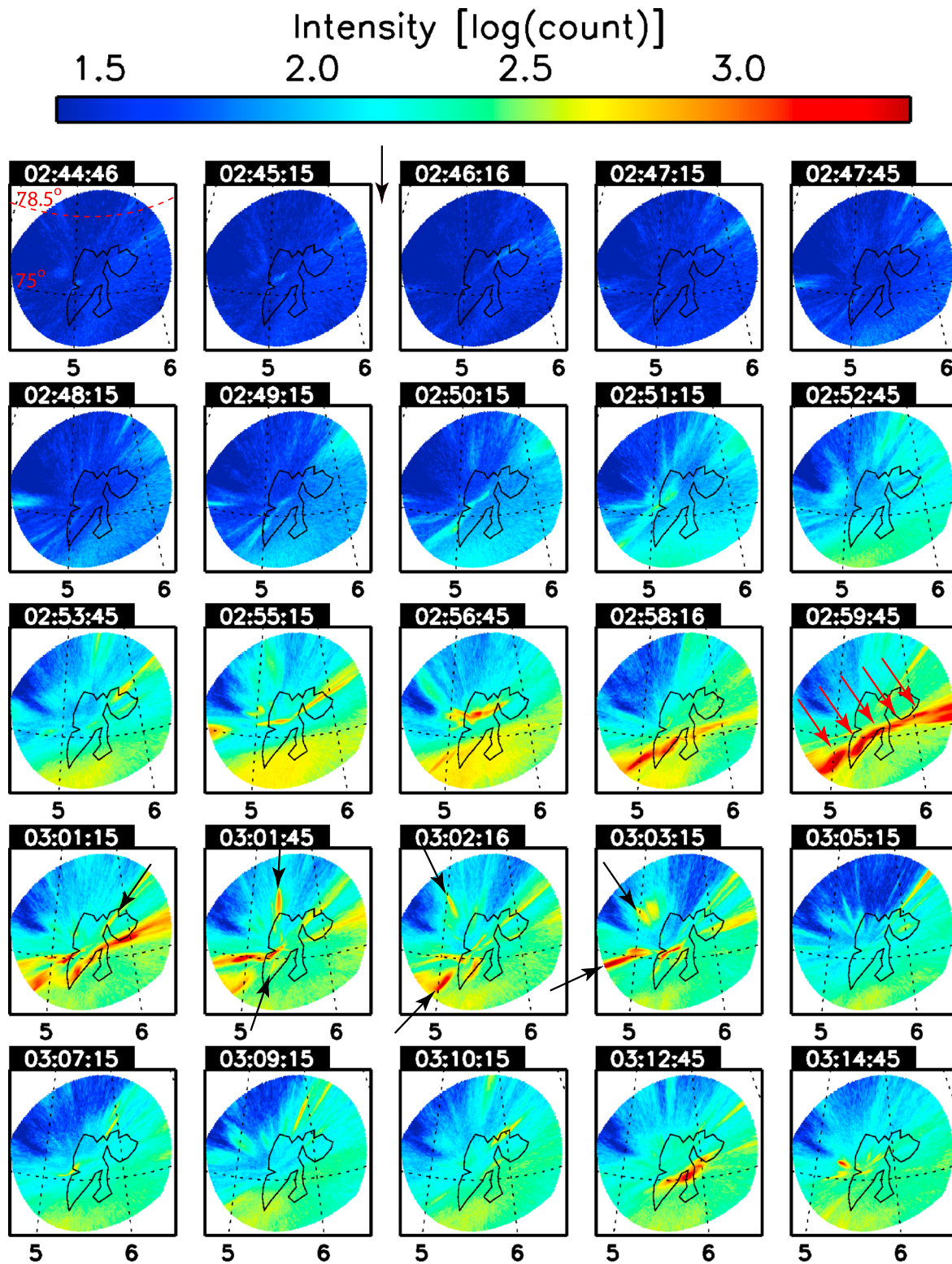


Figure 3. ASI images for the green emissions of the shock aurora event on 18 February 1999. The images are obtained from LYR at 75.2° MLAT and shown in the MLT-MLAT coordinates. The aurora was projected to 120 km altitude. The red dashed curve at 79.1° in the first image at 0244:46 UT marks the poleward boundary of the auroral oval identified using FAST data. The imager is not calibrated, and the color bar is for counts from $10^{1.4}$ to $10^{3.5}$. The black arrow in the top row shows the arrival time of the shock. Five red arrows in the image at 0259:45 UT indicate five streaks. Their moving speed is estimated after combining the information provided by the MSP scan (see more explanations in the text). The black arrows in the fourth row show that the streaks were moving from east to west, away from the Sun, no matter whether north or south of the zenith.

compression arrived at the magnetopause flank at ~ 6 MLT. From 0247:45 UT onward there were more intensified auroral streaks mainly in the northern sky and diffuse aurora in the south. Note that the streaks were mobile and moving fast toward the west, as marked by the red and black arrows on the third and fourth rows. From 0255:15 to 0303:15 UT, the auroral streaks became more intense and reached the saturation level of ~ 3200 counts. Five red arrows were used in the image at 0259:45 UT to mark five streaks that were moving roughly along 75° MLAT. Their propagation speed will be calculated when we discuss Figure 5. Their moving direction was similar to those marked by the black arrows on the fourth row, which were moving westward away from the Sun. Note that the farther the streaks were away from LYR, the longer lengths of the projections in the image due to the increased zenith angle. There seems to be an east-west "arc" in images 0258:16, 0259:45, and 0301:15 UT; these are illusions resulting from the connection or overlapping between projected streaks when occurring at similar latitude. The sketch in Figure 6 provides a better explanation for this situation.

Viewing aurora from LYR, the width of the streak varied from $\sim 2^\circ$ at ~ 280 km distance, corresponding to ~ 10 km (such as the one marked by the black arrow in the image at 0301:15 UT) to $\sim 5^\circ$ at ~ 350 km distance corresponding to ~ 30 km (such as the one marked by the black arrow in the west at 0303:15 UT). The average width of the streaks was about 20 km.

The diffuse aurora was propagating westward as well, although it was not seen in individual images. The diffuse aurora in the southern sky seemed suddenly intensified in one image from 0247:45 UT, which is due to the auroral area covered by ASI being much smaller in comparison to the entire oval and the ASI cadence being relatively slower in comparison to the auroral propagation speed. For example, for this particular event with a shock speed of $V_{sh} \sim 380 \text{ km s}^{-1}$ in the solar wind coordinates (using methods in Zhou and Smith [2015]), the shock propagation speed in the inertial coordinates was $V_{sw} \sim 980 \text{ km s}^{-1}$. Using the solar wind data at 0243 UT when IMF $B_z = 0$ nT and $P_{sw} = 1$ nPa as input to the Shue's model [Shue *et al.*, 1997], the calculated location of the dawnside magnetopause was $\sim 17 R_E$. As illustrated by the adiabatic compression effect [Zhou and Tsurutani, 1999], the diffuse aurora at 72° MLAT should propagate at the same angular speed with the shocks in the solar wind, and the propagation speed was found to be $\sim 18 \text{ km s}^{-1}$. In the span of 30 s, which is the highest cadence of the ASI images, the diffuse aurora should have propagated ~ 544 km from the magnetic east to west. While the diameter of the 557.7 nm images is ~ 820 km, the magnetic east-west distance along 72° MLAT of the image is ~ 363 km that is less than 544 km. This explains why the diffuse auroral propagation was not reflected in individual images. Instead, the entire southern sky was lit up and became brighter from one image to next.

Figure 4 displays the red emissions at 630.0 nm with the same format as in Figure 3 but projected to 250 km altitude. During the quiet time before 0247 UT, the red emissions showed similar structures as the green ones. Those were also streaks/rays, mainly along the northeast to southwest direction, though the red emissions at 630.0 nm were a little brighter, with ~ 400 to 500 counts compared with the green emissions displaying ~ 100 to 130 counts. After the shock arrival at ~ 0247 UT, the streaks were intensified. Corresponding to the five streaks in the green image at 0259:45 UT, four streaks were marked in the image at 0300:30 UT in which the most westward streak may have moved out from the FOV. The black arrows in the fourth row showed that the streaks were moving from east to west, away from the Sun as well.

Different from the green diffuse aurora intensified after 0247 UT, the red diffuse aurora in the southern sky was not evident until 0250 UT when the solar wind dynamic pressure was further enhanced to ~ 7 nPa. From 0253:30 to 0257:30 UT the red diffuse aurora became more intense and expanded from east to west through the southern sky. The intensity reached ~ 800 counts and above, which was similar to the green diffuse aurora at ~ 650 counts at 0256:45 UT. In 0256–0305 UT similar to the green streaks, there were short-lived red streaks moving along the east-west direction as well, but less intense at ~ 1300 counts. From ~ 0300 UT onward, a bright and wedge-shaped auroral emission occurred in the magnetic northeast when the solar wind dynamic pressure further increased and the IMF B_z started to turn from north to south. Shortly after that, the IMF B_y turned strongly duskward from ~ 10 to 20 nT, P_{ram} reached ~ 10 nPa, and B_z turned southward.

The MSP data for this 18 February 1999 event are shown in Figure 5 in which the top panel is for the green emissions and the middle for the red. The SI time at 0246 UT is marked by the arrow on the bottom of each panel. Very faint diffuse aurora in the green appeared in the southern sky at ~ 0247 UT and became evident around 0248 UT when some very faint diffuse red aurora started appearing in the south as well. Then, the

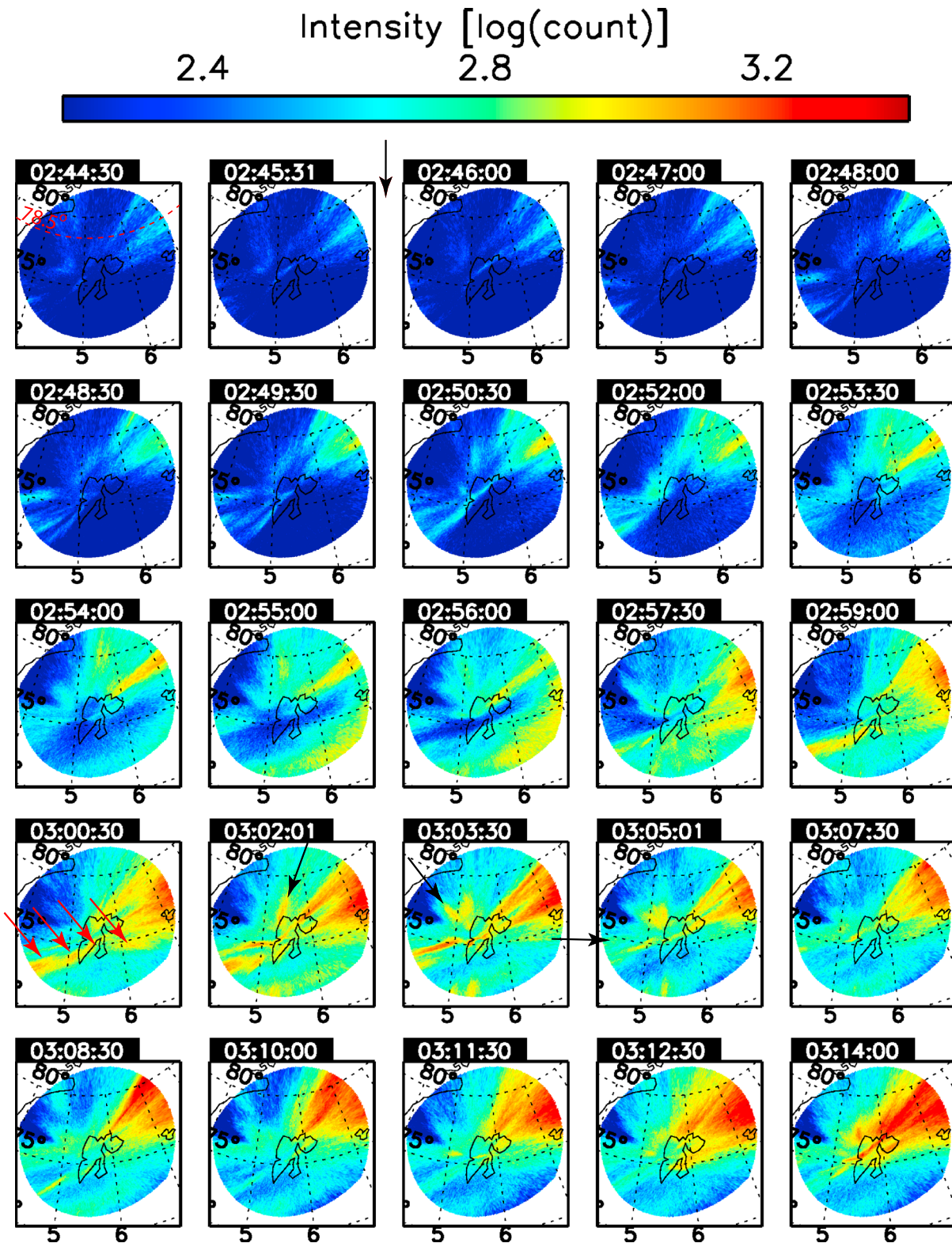


Figure 4. ASI images for red emissions of the shock aurora event on 18 February 1999. The figure has the same format of Figure 3, but the aurora was projected to 250 km altitude. The imager is not calibrated, and the color bar is for counts from $10^{2.2}$ to $10^{3.5}$. Four red arrows in the image at 0300:30 UT mark the streaks corresponding to those in Figure 3, but one of them had moved out of the FOV. The black arrows in the fourth row show that the streaks were moving from east to west, away from the Sun.

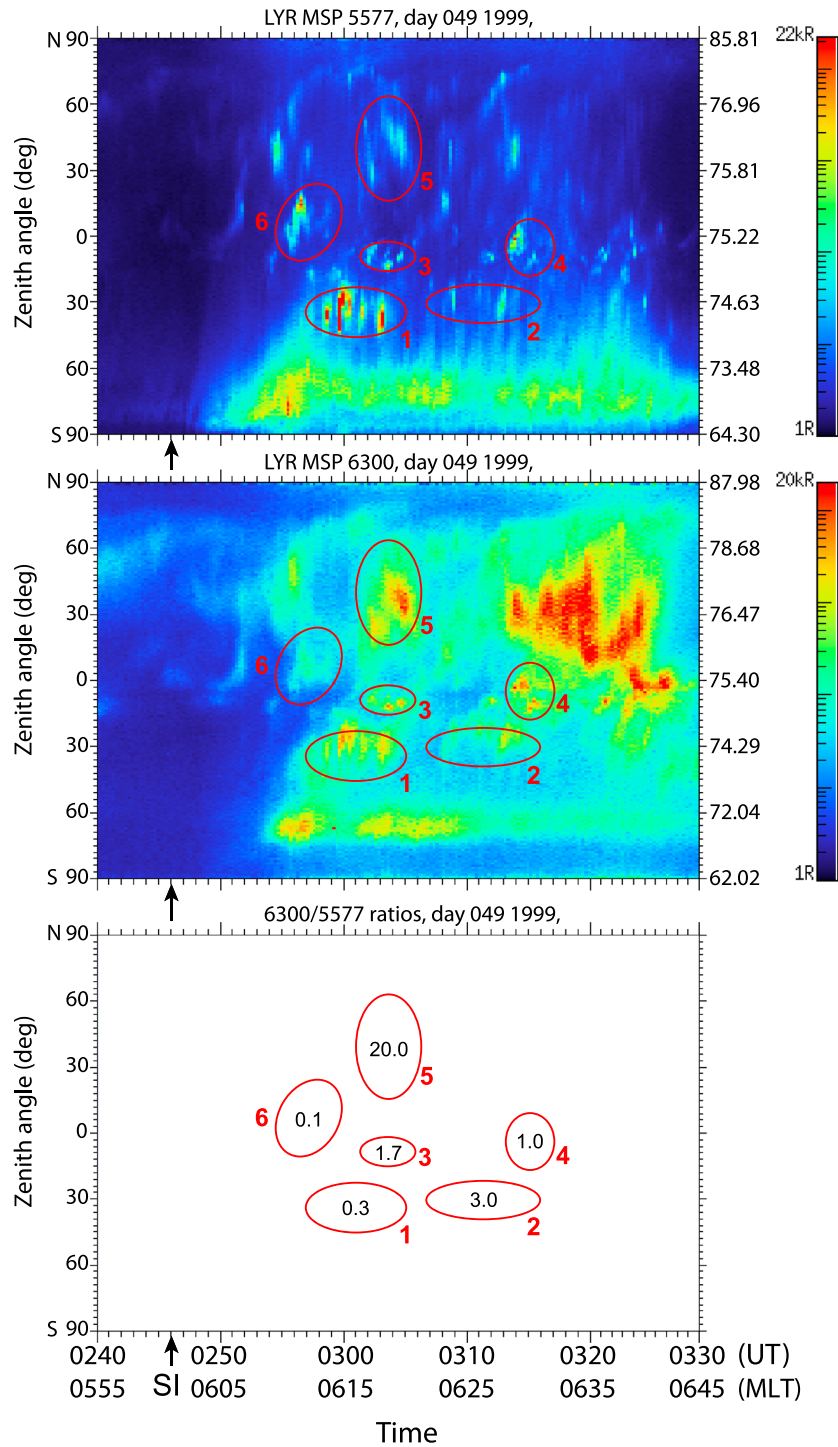


Figure 5. MSP of 18 February 1999 with the top panel for the green lines and the middle for the red lines. Arrows mark the SI time at 0246 UT. Y axis is the zenith angle on left and the magnetic latitude on right. The bottom panel contains the ratio between the respective brightness of 630.0 nm over 557.7 nm in the top two panels.

diffuse aurora propagated to higher magnetic latitudes, and by ~0257 UT the entire southern sky along the MSP path was covered by the diffuse aurora that had similar intensity in both green and red emissions. Although the lower latitude edge retreated after that time, the auroral intensity remained roughly the same until ~0340 UT when the solar wind dynamic pressure started reducing gradually.

To compare the discrete aurora in the green and red emissions, we group pairs of auroral stripes or dots in the MSP using circles and ovals. Each pair of ovals has identical shape and area size and covers the same time interval and zenith angles. For example, pair 1 starts from 0257 and ends at 0305 UT and from $S23^\circ$ to $S47^\circ$ zenith angle in both panels. Each pair contains stripes or dots from the same magnetic flux tubes, which occurred at the same time, but in different colors at different altitudes, therefore, different zenith angles. Such differences were very small at small zenith angles in pairs 3, 4, and 6 but were notable at large zenith angles in pairs 1, 2, and 5, where the red line emissions were not centered on the ellipses that corresponded to the green line emissions. The stripes in red emissions appeared closer to the zenith than those in green emissions because they were from higher altitudes on the same flux tube that were relatively far from the zenith comparing to those in pairs 3 and 4. These signatures suggested that the stripes were caused by electrons precipitating along same magnetic flux tubes, but with different energies. For those far from the local magnetic zenith (that is $\sim 9^\circ$ southward of the geographic zenith), the illuminated flux tubes were seen as a stripe, such as those in pairs 1, 2, and 5. For those close to or along the magnetic zenith the illuminated flux tube was viewed from below and, therefore, appeared as a bead or dot, such as those in pairs 3 and 4. (See the sketch in Figure 6 for further illustration.) Note that the auroral stripes and dots had very clear repetition in time, such as in pair 1, indicating moving flux tubes. Again, there was a lack of sharp structure in the red auroral streaks, which is because the red line at 630.0 nm is mainly caused by secondary electrons, and $O(^1D)$ atoms have a radiative lifetime of ~ 110 s [Rees *et al.*, 1967; Young and Black, 1967].

The narrowness of the streaks combined with their motion during the exposure plus calibration errors forbid determining trustworthy ratios between the red and green emissions. However, as rough indication it may be quite valuable. This has been done and shown in the lower panel of Figure 5, in which the ratio between the respective brightnesses in 630.0 nm and 557.7 nm in each pair is given in the corresponding circle. The low ratios in pairs 6 and 1 would be consistent with average energies between ~ 2 and ~ 1 keV, respectively, according to Figure 5 in Rees and Luckey [1974]. This means that postacceleration above the ionosphere by parallel potential drops is not in conflict with the optical data. Note that since there was a saturation of the streak intensity in circle 1', the ratio of circle 1 may well be below 0.1. So the energy can be higher than 2 keV. All other pairs are dominated by soft electron spectra.

The streak moving speed can be estimated using streaks in Figure 3 and circle 1' in Figure 5. The five streaks marked in the image at 0259:45 UT in Figure 3 passed the MSP's FOV from $\sim 0258:30$ to $0303:30$ UT along $\sim 74.6^\circ$ MLAT. As seen in the images from 0258:16 to 0303:15 UT, the streaks moved cross the ASI's FOV of ~ 2 h in MLT from east to west. Therefore, the streaks' speed in the ionosphere is ~ 3.0 km s^{-1} . Using the same angular speed, the corresponding speeds mapped to the dawnside magnetopause at $\sim 12 R_E$ were ~ 133 km s^{-1} , which was consistent with the observed speeds of magnetopause surface waves at ~ 65 – 200 km s^{-1} . The waves were measured by Cluster and were attributed to the Kelvin-Helmholtz instability [Owen *et al.*, 2004; De Keyser *et al.*, 2004]. Also based on the five streaks marked in the image at 0259:45 UT in Figure 3, the distance between the streaks was roughly ~ 180 km, on average.

4. Discussions

UV auroral imaging from space first revealed the large-scale dynamics of the shock aurora, such as the local time of the auroral onset, the auroral expansions in latitudinal and longitudinal directions, and the auroral propagation speed in the ionosphere. The most relevant mechanism is the adiabatic compression [Zhou and Tsurutani, 1999]. With increasing knowledge about the different forms of the shock aurora, we learned that magnetic reconnection and Alfvén waves play important roles as well around local noon [Zhou *et al.*, 2003, 2009, 2010]. Using the ground-based auroral measurements at ~ 06 MLT, this paper allowed an insight into the dawnside shock aurora that exhibits ionospheric manifestations of magnetic and velocity shearing along the flanks of the magnetosphere. The findings of this study may have revealed an important mechanism for discrete aurora on the dayside dawn and dusk sectors. However, deliberate discussions are necessary to correctly understand and explain what the measurements presented above indicate and suggest.

4.1. The Poleward Boundary of the Auroral Oval

It is important to verify that the largest portion of the ASI images in Figures 3 and 4 was within the auroral oval, but not in the polar cap, because streaks in the images were used to estimate their moving speed, such as those in the image at 0259:45 UT. This ionospheric speed was later found to match with the speed of the

surface waves along the magnetopause flank, which became an important argument of our speculation; that is, the fast and tailward moving streaks may be the ionospheric manifestation of the magnetic field and flow shears at LLBL, which can be intensified under interplanetary shock compression.

While no Polar/UVI and IMAGE/FUV images were available for this shock event, there were FAST data of two crossings of the dawnside auroral oval in the Northern Hemisphere about 1 h before and 1 h after the SI. The data were very helpful in identifying where the poleward boundary of the oval was, because the solar wind was quiet several hours in the shock upstream. Interested readers can find the FAST data in the supporting information.

The FAST magnetic field and particle data of orbit 9862 showed that at ~ 0117 UT the poleward boundary of the oval was at $\sim 78.5^\circ$ MLAT, below which there were continued electron and high-energy ion precipitations, implying that LYR (at $\sim 75.2^\circ$ MLAT) was $\sim 3^\circ$ latitudes below the boundary. As shown in Figure 2, the upstream solar wind and northward IMF conditions were stable, and the IMF turned more northward at the shock to cause the boundary to move even more northward. Therefore, it is very likely that LYR remained $\sim 3^\circ$ or even more below the boundary until the IMF B_z turned to deep southward at ~ 0315 UT. For the given ASI/FOV of 150° , the highest latitude that the auroral images could reach is 78.8° MLAT at the altitude of 110 km and 79.1° MLAT at 120 km. That is to say that almost the entire auroral image of the green emissions shown in Figure 3 was not showing the cap, except for the northern tip, but within less than 1° MLAT.

The FAST data of orbit 9863 showed that at ~ 0333 UT, LYR (at 75.2° MLAT) was still below, but very close to the poleward boundary that was at 75.7° MLAT. Note that by then, the IMF B_z was about -20 nT, and the oval had moved equatorward after the deep southward turning at ~ 0315 UT. Evidently, orbit 9863 observations also supported the conclusion that the auroral streaks discussed for Figures 3 and 4 were below the poleward boundary and were in the area of the ionospheric footprints of the LLBL, especially those streaks around and below the zenith.

4.2. Auroral Streaks Versus Auroral Arcs

The ASI records the three-dimensional auroral dynamics onto a two-dimensional image, while the MSP monitors the time variation of a $\sim 1^\circ$ wide slice of the sky from north to south along the magnetic meridian. They both have limitations by default, which can be minimized when the two data sets are combined for analysis. A good example is shown in Figure 6 that explains how to identify discrete aurorae as auroral streaks or auroral arcs. Instead of showing a single wavelength separately like in Figures 3–5, here we use white light that combines separated features into one to depict the height and distance effect of vertical structures. When the red and green objects are in the same frame, those differences are easily compared. The sketch on the left explains why in the ASI image a discrete segment does not necessarily mean an auroral arc. It is actually a little bit tricky to extrapolate the auroral morphology in the sky based on the auroral forms reflected in the image. Shown in the left that is assumed to be taken from t_1 to t_4 using the same exposure time, three streaks S_1 – S_3 present illuminated individual magnetic flux tubes aligned with the magnetic meridian, and an arc A_4 is the horizontal trace representing the ionospheric footprint of a field-aligned current sheet that is east-west aligned. All of their projections (except S'_1) in the ASI image have certain length and look like arcs but with some uncertainty due to the orientation of S'_2 and S'_3 as well as their type of a straight line.

Fortunately, when combining ASI data with MSP scans, some ambiguity can be clarified. For example, when S_1 – S_3 move westward as indicated by the three black arrows in the left and pass the MSP's FOV at t_1 – t_3 , they appear to be like S_1 – S_3 in the right panel, which locations in zenith are determined by z_1, z_2, z_3 and z'_1, z'_2, z'_3 that are measured in the left. The red emissions are on top of the green emissions in altitude and, therefore, have smaller zenith angles along stripes S_2 and S_3 that are far from the magnetic zenith, but no difference for S_1 because it is along the magnetic zenith. This explains why in the middle panel of Figure 5, in circles 1, 2, and 5 the 630.0 nm stripes appeared at smaller zenith angles relative to the circle center where the 557.7 nm stripes occurred, but such a difference is not seen in circles 3 and 4. Since A_4 in the left panel is moving southward, and its zenith angle decreases from t_3 to t_4 , A_4 in the right can be a smooth curve as shown or can be a more complicated curve or a simple straight line from (t_3, z_4) to (t_4, z'_4) depending on the dynamics of the current sheet.

When the same streaks in the left are aligned in the east-west direction also with S_1 along the magnetic zenith, the projections S'_2 and S'_3 in the ASI image will look like east-west oriented "arcs," but their

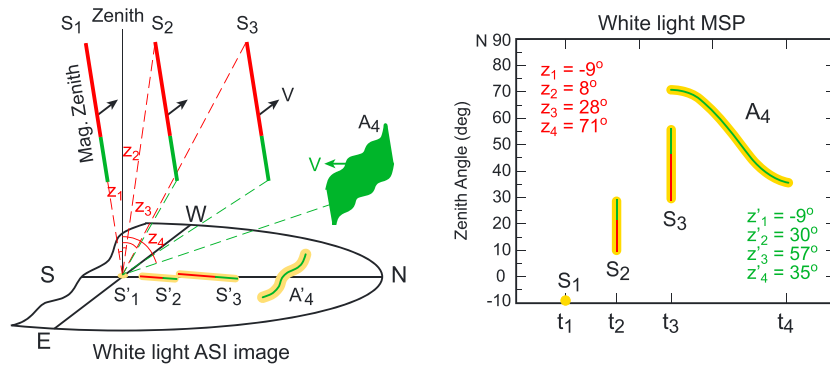


Figure 6. Auroral streaks and arcs in ASI and MSP. The sketches, which are not to scale, illustrate how the combination of ASI images and MSP scans can reveal auroral signatures and dynamics that cannot be achieved using only one type of the observations. The left panel illustrates what streaks and arcs may look like in a white light ASI image in which the magnetic north (N) to the right, and only half image of the northern sky is drawn for simplicity. S_1 – S_3 mark three identical streaks with the red emissions above the green, and all are moving westward as shown by the three black arrows. But the three streaks pass the magnetic meridian (i.e., the MSP scan path) at t_1 , t_2 and t_3 , respectively. In the ASI image that assumed is taken using an exposure time from t_1 to t_4 , S'_1 – S'_3 in orange represent projections in the white light of S_1 – S_3 but may be dominated by the red or green emissions at different portion, as shown by the overlapped red and green lines. S_1 is a streak along the magnetic zenith that is $\sim 9^\circ$ south of the geographic zenith, so its zenith angles z_1 , from the streak top, and z'_1 , from the streak bottom, are the same at -9° ; the other two streaks have some distance from the zenith; therefore, the top and bottom of the streaks are at different zenith angles, as shown by the red and green dashed lines and labels. An east-west oriented green arc is marked as A_4 in the sky, and its projection is A'_4 in the image. An arc is actually the ionospheric trace of a current sheet, such as the popular and visible ones in the 557.7 nm around 120 km altitude and the 630.0 nm around 250 km. A_4 moves southward as indicated by the green arrow from z_4 to z'_4 , but z'_4 is not marked. Note that S'_1 looks like an auroral spot because it is along the magnetic zenith, while when far from the magnetic zenith, S'_2 and S'_3 look like a N-S oriented auroral arc with certain length. The right panel is a white light MSP scan for the sky in the left panel depicting the three streaks that occur at t_1 – t_3 and the arc A_4 lasts from t_3 to t_4 while moving southward. The given zenith angles in the upper left and lower right corners are measured from the red and green dashed lines in the left panel except z'_4 that is a given value. The red emissions at higher altitude have lower zenith angle in MSP and the green emissions at lower altitude with higher zenith angle, as shown by the red and green lines overlapping with the white light stripes. For the same reason, circles 1, 2, and 5 appeared at high zeniths in the middle panel of Figure 5. Similar to the streak projections in the ASI image on left, the length of S_1 – S_3 in the MSP scan increases with their increasing zenith angle.

appearances in the MSP scan will be three dots at t_1 , t_2 , and t_3 at zenith angle = -9° , which clarifies that those east-west oriented arcs in ASI are fake ones. This is the situation shown in circles 3 and 4 in Figure 5 and images around 0303:15 UT in Figure 3 and 0303:30 UT in Figure 4 when there were streaks closely aligned with the magnetic zenith latitude at $\sim 75^\circ$ MLAT. When the east-west aligned streaks S_1 – S_3 are away 75° MLAT, their appearances in the MSP scan will be three stripes at t_1 , t_2 , and t_3 , which are similar to those in circles 1, 2, 5, and 6. In particular, stripes in circle 1 are what we are seeing in images around 0259:45 UT in Figure 3 and around 0300:30 UT in Figure 4. In addition, it is worth pointing out that as the footprint of current sheets, arcs are embedded with wiggling and waving structures, which are not seen in the discrete aurorae in Figures 3 and 4. In contrast, streaks in ASI are straight line segments and roughly along the radial direction of the image, which are the dominant signatures in the ASI data for this event.

For readers who prefer using ASI images, a raw image of the green emission at 0259:45 UT is enclosed in the supporting information. The image shows more discreteness without the distortion when projected into the geomantic coordinates. But readers should view the image with caveats because it is not calibrated and in a different orientation.

4.3. LLBL Vortices and the Field-Aligned Potential Drop

It is tempting to identify the narrow short-lived vertical structures/streaks, prominent in the ASI images after the shock arrival at ~ 0246 UT, especially between 0255 and 0315 UT as shown in Figures 3–5, as traces of vortices forming along the dawnside magnetopause. Such vortices are thought to evolve from Kelvin-Helmholtz waves at the flanks of the magnetopause under northward IMF B_z conditions. They have been observed by Cluster [De Keyser et al., 2004, 2005; Hasegawa et al., 2004; Owen et al., 2004] and treated theoretically by

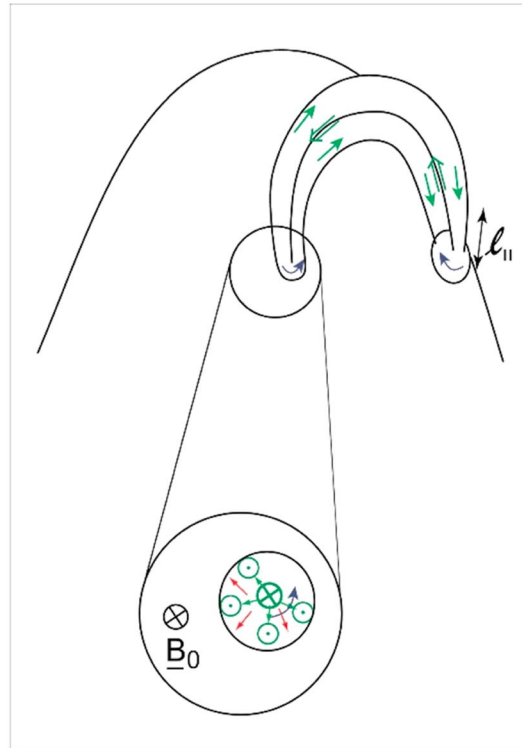


Figure 7. Cartoon of the connection between the nonlinear structure at the magnetopause and the polar ionosphere indicates the latitudinal extent of the momentum influx along the magnetopause. Green arrows indicate currents which connect to the field-aligned currents, in the ground projection marked by green circles. Red arrows indicate the electric fields of $-\mathbf{V} \times \mathbf{B}$.

simulations [e.g., Miura, 1992; Nakamura et al., 2004]. In situ observations on the magnetopause boundary showed that the vortices may be effective in mixing magnetosheath with magnetospheric material, possibly aided by cascading to small scales and reconnection. However, the observed structures during the shock compression may rather correspond to large-amplitude structures formed inside a shear flow layer and appearing as beads, similar to the ones observed at substorm onset near midnight [Liang et al., 2008; Sakaguchi et al., 2009; Rae et al., 2009; Hosokawa et al., 2013]. The ASI images and MSP traces in this study showed the stripe-type structures in both 557.7 and 630.0 nm emissions. Such sheared structures would transfer magnetic shear stresses along magnetic flux tubes of limited cross section. Therefore, the question arises whether the auroral emissions were caused by the dumping of Alfvén waves or the precipitation of post-accelerated electrons in the attending upward field-aligned currents. Since we lack direct measurements from

above the ionosphere, we will address this question by evaluating the images in the framework of some theoretical concepts. We approach the situation from two ends. First, we look at the generation of shear stresses in the boundary layer and derive therefrom the field-aligned currents carrying the stresses and related Poynting flux downward. Mapping the currents into the ionosphere gives a measure of the arriving energy flux, which will then be balanced with the energy flux of precipitating electrons, as derived from the optical data.

Nonlinear wave structures or vortices are formed by a balance between mechanical momentum flux absorbed from the external flow and magnetic shear stresses on the inside. However the detailed configuration looks like, we can cast it into the simple balance equation:

$$\alpha \rho_{\text{msh}} V_{\text{msh}}^2 = s_b j_{\perp} B_{\text{MP}}, \tag{1}$$

ρ_{msh} is the density in the magnetosheath and V_{msh} the flow velocity. $\alpha \ll 1$ [Miura, 1992] is a constant representing the effective viscosity responsible for the nonlinear growth of the surface waves and the related momentum transfer to the magnetosphere. j_{\perp} and B_{MP} are the current and magnetic field of the Lorentz force acting against the transferred mechanical stress at the magnetopause, and s_b is the braking length of the flow generated inside the nonlinear structure. Figure 7 provides a simple illustration. One notices the opposing direction of transverse current and electric field in the figure, indicating the generation of balanced upward and downward currents. The mechanical stress is applied over a latitudinal extent, $2\ell_{\parallel}$. We consider solely the momentum transfer without touching on the difficult problem of reconnection to the external field [Hasegawa et al., 2004; Nakamura et al., 2004]. The magnetic shear stresses are propagated in the Alfvén mode along the internal field and a field-aligned sheet current arises from the divergence of j_{\perp} :

$$J_{\parallel} = j_{\perp} \ell_{\parallel} = \frac{\alpha \ell_{\parallel}}{s_b} \cdot \frac{\rho_{\text{msh}} V_{\text{msh}}^2}{B_{\text{MP}}}. \tag{2}$$

It is the upward leg of the attending field-aligned currents where is well above the ionosphere energy conversion and downward electron acceleration would take place, which would give rise to auroral emissions. The field-aligned sheet current density in the ionosphere would be as follows:

$$J_{\parallel, \text{ion}} = \sqrt{\frac{B_{\text{ion}}}{B_{\text{MP}}} \frac{\alpha \ell_{\parallel}}{s_b} \cdot \frac{\rho_{\text{msh}} V_{\text{msh}}^2}{B_{\text{MP}}}} \quad (3)$$

$\mu_0 J_{\parallel, \text{ion}}$ would be the magnetic perturbation field, B_{\perp} , just above the energy conversion region. This could be either the topside ionosphere for Alfvén waves or the auroral acceleration region for quasi-stationary currents.

Equation (3) is a simple formula for the generation of current along a sheared flux tube underneath a vortex or other type of nonlinear structure formed at the magnetopause. The magnetospheric field inside the sheared flux tube guides the Poynting flux earthward and, depending on the duration of the energy input, stores energy inside the flux tube. If we regard the twisted flux tube as an entity created and decaying and not as a stationary current source, we can relate the energy flux into the auroral ionosphere as the ratio of stored energy and decay time, τ_d . Using an expression for the stored energy from *Haerendel* [2012],

$$W_{\text{vort}} = \frac{B_{\perp}^2}{2\mu_0} \cdot \ell_{\text{eff}} \quad (4)$$

with $\ell_{\text{eff}} = 2R_E L / \Gamma^2$ being the effective length of the twisted flux tube. $R_E L$ is the equatorial distance of the vortex and a Γ^2 parameter of order unity arising from the distorted field model, we can now express B_{\perp}^2 by equation (3) and evaluate equation (4) by adopting the following quantities, largely based on observations on average: $V_{\text{msh}} = 400 \text{ km s}^{-1}$, $n_{\text{msh}} = 6 \text{ cm}^{-3}$, $B_{\text{MP}} = 35 \text{ nT}$, $B_{\text{ion}} = 0.54 \text{ G}$, $\dot{W}_{\text{vort}} = W_{\text{vort}} / \tau_d = 40 \text{ mW/m}^2$, $\tau_d = 1 \text{ min}$, and $L = 14$. The energy flux of 40 mW/m^2 was derived from a photon flux of $\sim 14 \text{ kR}$ at 557.7 nm (such as streaks in circle 1 of Figure 5). To ensure that those numbers are reasonable, we have checked Time History of Events and Macroscale Interactions during Substorms (THEMIS) observations for a similar event on 19 November 2007, i.e., THEMIS/THC was crossing the dawnside magnetopause when an interplanetary shock arrived. The shock upstream conditions are similar to this 18 February 1999 shock with a stable northward IMF B_z at $\sim 2 \text{ nT}$ for $\sim 3 \text{ h}$ in the upstream and the solar wind velocity at $\sim 400 \text{ km s}^{-1}$. The shock caused a sudden impulse at $\sim 1811 \text{ UT}$ on 19 November 2007. Observations in 1710–1830 UT from the ESA instrument on board THEMIS/THC can be found in the supporting information. The figure shows that N_p varied from ~ 5 to 11 cm^{-3} , the velocity along the magnetopause varied around 300 km s^{-1} , and the total magnetic field was ~ 20 – 25 nT . Interestingly, the figure also shows a rippled magnetopause boundary even before the shock arrival. However, the spacecraft was exposed to the sheath due to the shock compression, indicating that the opportunity to observe KH waves or vortices on LLBL at the shock arrival is very low. On the basis of the shock downstream conditions, the velocity and magnetic shears were definitely enhanced. One can reasonably assume that KH waves or vortices along the magnetopause were formed or increased as well.

With $\varepsilon = \frac{\alpha \ell_{\parallel}}{s_b}$ we get from equation (3): $J_{\parallel, \text{ion}} = \varepsilon \cdot 1.75 \text{ A/m}$ and $B_{\perp} = \varepsilon \cdot 2.2 \cdot 10^{-2} \text{ G}$. From equation (4) and $W_{\text{vort}} = \dot{W}_{\text{vort}}$ one finds: $B_{\perp}^2 = 5.07 \cdot 10^{-6} \text{ G}^2$. Balancing the two expressions yields: $\varepsilon = \frac{\alpha \ell_{\parallel}}{s_b} = 0.1$. Looking at equation (3), we see that ε is nothing else than the magnetic viscosity. The magnitude of ε is thus not far from the $0.05 M_s^{-2}$ derived by *Miura* [1992]. Finally, the field-aligned current density for an effective cross section of $\sim 20 \text{ km}$ in the ionosphere (as an average based on the estimations from Figure 3) turns out to be $8.8 \times 10^{-6} \text{ A/m}^2$. This is distinctly higher than the current density derived for Alfvénic arcs by *Haerendel and Frey* [2014], as are the photon and deduced energy fluxes. But the field-aligned potential drop corresponding to the above values of energy flux and current density turns out to be $4.6 \pm 1.1 \text{ kV}$, if the effective cross-section changes in a range of $20 \pm 5 \text{ km}$. This potential drop is reasonably consistent with the observations, although a bit on the high side. With all caution in view of the simplicity of our above analysis, one may thus take this finding as suggesting that the electrons carrying the current inside the sheared flux tubes are in all likelihood postaccelerated by the field-parallel potential drop.

An important finding is that the spatial scales used in the above analysis are about one order of magnitude smaller than the vortices derived from Cluster measurements by *Hasegawa et al.* [2004]. This follows from the typical separation of two adjacent streaks, if identified as images of nonlinear KH waves. The separation length, observed to range between 80 and 170 km, would map into a typical separation of ~ 0.5 – $1.0 R_E$ at the magnetopause. Using the common ratio of eight between KH wavelength and width of the shear

layer, the latter would range between 400 and 800 km. This is consistent with the typical width of the magnetopause [Paschmann *et al.*, 2005] and, if projected into the ionosphere, corresponds to the widths of the observed streaks at ~10–20 km. These widths are quantitatively consistent with observations shown in Figure 3. The auroral streaks are therefore nonlinear structures inside the dawn magnetopause. They are obviously of very different nature than the vortices observed by Cluster. Our interpretation implies a viscous interaction between magnetosheath flow and magnetosphere of the kind discussed by Miura [1992] and by Sonnerup [1980] for the low-latitude boundary layer. Notwithstanding the uncertainties involved in the above estimates, we can derive from equation (3) an expression for the magnetic viscosity, $\nu_{van} = \varepsilon \cdot a V_{msh}$, with $\varepsilon \approx 0.1$ and a being the thickness of the shear layer. The magnitude of ε is close to the theoretical result of Miura [1992] for low sonic Mach number. However, our findings are for a different reason inconsistent with Miura's theory, since for $M_s = 1.0$ he obtains vortices of much greater extent than the thickness of the shear layer. The fact that the structures forming in our case are much narrower is probably due to the rather high magnetic viscosity of the order of 10^{14} cm²/s. This surprising finding may be owed to the special situation created by the passage of the shock front.

The question is then whether the observed streaks are a product of the shear stresses released inside the auroral acceleration region [Davis, 1978] or images of KH waves generated at the magnetopause. In the first case we would expect a much more regular pattern like auroral rays in active arcs and also much shorter separation lengths. The streaks observed here are more reminiscent of the beads observed at substorm onset [Liang *et al.*, 2008; Sakaguchi *et al.*, 2009; Rae *et al.*, 2009; Hosokawa *et al.*, 2013]. Furthermore, quite alike to our situation, appearance of the auroral beads seems to be invariably connected with fast, mostly eastward, but occasionally also westward flows in the tail plasma sheet. In both cases, at substorm onset in the midnight sector as well as at the morning flank of the magnetopause during shock passage, nonlinear KH waves may thus be excited. While the former is found to appear in the ionosphere by precipitation of soft electron fluxes (<1 keV), the latter seem to be connected with high current densities and more energetic electron fluxes.

Finally, we can obtain an estimate on the momentum coupling parameter, α , used in equation (1). If we assume that the braking length, s_b , is of the order of the KH wavelength, i.e., $\sim 1 R_E$, and ℓ_{\parallel} a few Earth radii, we find $\alpha \leq 0.03$. This looks fairly reasonable. However, we do not exclude that the first case may occur as well during the shock compression.

4.4. Discrete Shock Auroras at Local Noon and Dawnside Auroral Oval

Comparing the shock aurora event at local noon [Zhou *et al.*, 2009] to this event, the most striking difference is that the green and red auroras were caused by two separate mechanisms near local noon, but by the same mechanism at dawnside. Near local noon, the green and red auroras were mainly separated in location and basically different in forms, which imply that there were two major populations of the precipitating electrons. One was the isotropic hard electrons with energy above 1 keV. They were mainly on closed field lines. The other one was field-aligned soft electrons with energy below 1 keV (Alfvénic electronic electrons) along the open-close field line boundary or in the cusp. By contrast, at the dawnside of the oval the green and red auroras coincided in location and form, i.e., intense diffuse aurora and distinct auroral streaks occurred in both green and red at the same time. Those coexisting auroral rays/streaks may very well be the ionospheric manifestation of KH waves on the flank magnetopause generated by velocity and magnetic shears and Kelvin-Helmholtz instability, the shears can drive intense field-aligned currents into the ionosphere, as described in the previous section. The distinction in the discrete aurora suggests that the driven mechanisms are highly local time dependent.

4.5. The Stretching Cusp

During the event the cusp may have moved to ~06 MLT as shown in Figures 4 and 5, especially in the 630.0 nm MSP scan after 3015 UT. There might be two causes for this extreme situation. One is the sudden enhanced solar wind pressure that can enlarge the cusp width, and the other is the large positive IMF B_y , that can shift the cusp downward. Polar observations show that the cusp location varies in ~08–16 MLT, and it becomes wider when solar wind dynamic pressure increases [Russell, 2000; Zhou *et al.*, 2000]. In addition, the cusp location is apparently controlled by the interplanetary magnetic field orientation. When the IMF B_y is positive, the cusp location will move to westward [e.g., Newell *et al.*, 1989; Moen *et al.*, 1999; Lockwood *et al.*, 2003]. Moen *et al.* [2001] probed cusp in the late dusk sector to 1630 MLT, and Milan *et al.* [2000]

reported dusk cusp signatures all the way into the 19 MLT sector. For this particular event, besides a dynamic pressure increase from ~ 1 to 6 nPa at the shock, the IMF B_y turned to more positive from ~ 5 to 7 nT at the shock and increased to ~ 22 nT at ~ 0305 UT. With this extreme large duskward IMF B_y and abruptly enhanced solar wind dynamic pressure, one can expect a widened and westward shifted cusp. Therefore, both mechanisms may have acted and placed the morning end of the cusp at ~ 06 MLT.

5. Summary and Conclusion

We have examined a shock aurora event recorded by the ground-based ASI and MSP at ~ 06 MLT. In addition to the diffuse aurora (in both green and red), auroral streaks/rays moving tailward along the poleward boundary of the auroral oval were observed in all wavelengths (also in the purple emissions at 427.8 nm, not shown in this paper). Note that the shock aurora at dawnside is very different from that near local noon where the shock-generated red and green emissions occurred in different locations and forms [Zhou *et al.*, 2009].

These discrete vertical auroral structures are believed to be ionospheric ends of moving flux tubes illuminated by postaccelerated precipitating electrons. The speeds of the streaks were ~ 3 km s $^{-1}$ in the ionosphere, which corresponds to ~ 133 km s $^{-1}$ on the dawnside magnetopause. The speeds are consistent with the speeds of surface waves of ~ 65 km s $^{-1}$ [Owen *et al.*, 2004] and ~ 200 km s $^{-1}$ [De Keyser *et al.*, 2004] observed at the flank magnetopause and were attributed to the Kelvin-Helmholtz instability. However, the wavelengths of ~ 0.5 – $1.0 R_E$ found in our event are substantially shorter than these surface waves that are closer to the scale of vortices of Hasegawa *et al.* [2004].

Assuming that the auroral streaks are the ionospheric manifestation of nonlinear waves on the flank magnetopause due to the Kelvin-Helmholtz instability, we have estimated the field-aligned current density by balancing the mechanical momentum flux at the magnetopause with the magnetic shear stresses transferred toward the ionosphere, whereby the latter were derived from estimates of the energy flux deduced from the observed brightness of the streaks. The current density is found to be $\sim 8.8 \times 10^{-6}$ A/m 2 , which is distinctly higher than the current density derived for Alfvénic arcs [Haerendel and Frey, 2014], suggesting that the electrons carrying the current inside the sheared flux tubes are postaccelerated by a field-parallel potential drop. But correspondingly, the field-aligned potential drop is $\sim 4.6 \pm 1.1$ kV, if the effective cross-section changes in the range of 20 ± 5 km. In spite of the inherent uncertainties, the ratios of the brightnesses at 630.0 nm over 557.7 nm are consistent with a substantial contribution of electrons above 1 keV. As a matter of fact, this shock-generated field current was recorded by the ground-based IMAGE magnetometer chain as a couple of reversed vortices in the equivalent current, indicating the opposite direction of the ionospheric convection. The corresponding Polar plots are from SuperMAG and are enclosed in the supporting information.

A surprise is the spatial scale derived for the KH wavelengths from upward mapping of the observed auroral streaks. They turn out to be about one order of magnitude smaller than the scale of vortices encountered by the Cluster mission. The streaks are therefore not images of vortex formation in the magnetosphere but of nonlinear waves generated inside the magnetopause layer. The 400 km width of the shear layer, derived from the wavelength, times the speed of the magnetosheath flow implies an anomalous viscosity of $\sim 10^{14}$ cm 2 /s generally consistent with the theories of Sonnerup [1980] and Miura [1992] but with a somewhat higher magnitude.

References

- Araki, T. (1994), A physical model of the geomagnetic sudden commencement, in *Solar Wind Sources of Magnetospheric Ultra-Low-Frequency Waves*, edited by M. J. Engebretson, K. Takahashi, and M. Scholer, pp. 183–200, AGU, Washington, D. C.
- Cassak, P. A., and M. A. Shay (2007), Scaling of asymmetric magnetic reconnection: General theory and collisional simulations, *Phys. Plasmas*, *14*, 102114.
- Chaston, C. C., et al. (2005), Drift-kinetic Alfvén waves observed near a reconnection X line in the Earth's magnetopause, *Phys. Rev. Lett.*, *95*, 065002, doi:10.1103/PhysRevLett.95.065002.
- Craven, J. D., L. A. Frank, C. T. Russell, E. E. Smith, and R. P. Lepping (1986), Global auroral responses to magnetospheric compressions by shocks in the solar wind: Two case studies, in *Solar Wind-Magnetosphere Coupling*, edited by Y. Kamide and J. A. Slavin, pp. 367–380, Terra Sci., Tokyo.
- Davis, T. N. (1978), Observed characteristics of auroral forms, *Space Sci. Rev.*, *22*, 77–113, doi:10.1007/BF00215814.
- De Keyser, J., G. Gustafsson, M. Roth, F. Darrouzet, M. Dunlop, H. Rème, A. Fazakerley, P. Décréau, and N. Cornilleau-Wehrin (2004), Reconstruction of the magnetopause and low latitude boundary layer topology using Cluster multi-point measurements, *Ann. Geophys.*, *22*, 2381–2389, doi:10.5194/angeo-22-2381-2004.

Acknowledgments

We gratefully acknowledge the CDAWeb for access to t–he OMNI solar wind data (http://omniweb.gsfc.nasa.gov/form/omni_min.html) and the WDC for Geo-magnetism at Kyoto University (<http://wdc.kugi.kyoto-u.ac.jp/index.html>) for making SYM-H, AU, and AL indices available to public access. We acknowledge NASA contract NAS5-02099 and Vassilis Angelopoulos for use of data from the THEMIS Mission. We acknowledge SuperMAG and Jesper Gjerloev for use of Polar plots of the ground magnetometer data. The UiO all-sky imager network is supported by the Research Council of Norway contract 230935. Xiaoyan Zhou thanks Margaret Kivelson and James Weygand for their helpful discussions. Auroral ASI images are provided by Lasse Clausen lasse.clausen@fys.uio.no, MSP data by Dag Lorentzen at dag.lorentzen@unis.no, and FAST data by Robert Strangeway at strangeway@igpp.ucla.edu.

- De Keyser, J., M. Roth, M. W. Dunlop, H. Rème, C. J. Owen, and G. Paschmann (2005), Empirical reconstruction and long-duration tracking of the magnetospheric boundary in single- and multi-spacecraft contexts, *Ann. Geophys.*, *23*, 1355–1369, doi:10.5194/angeo-23-1355-2005.
- Erlanson, R. E., and L. J. Zanetti (1998), A statistical study of auroral electromagnetic ion cyclotron waves, *J. Geophys. Res.*, *103*, 4627–4636, doi:10.1029/97JA03169.
- Erlanson, R. E., L. J. Zanetti, T. A. Potemra, M. André, and L. Matson (1988), Observation of electromagnetic ion cyclotron waves and hot plasma in the polar cusp, *Geophys. Res. Lett.*, *15*, 421–424, doi:10.1029/GL015i005p00421.
- Fairfield, D. H., A. Otto, T. Mukai, S. Kokubun, R. P. Lepping, J. T. Steinberg, A. J. Lazarus, and T. Yamamoto (2000), Geotail observations of the Kelvin-Helmholtz instability at the equatorial magnetotail boundary for parallel northward fields, *J. Geophys. Res.*, *105*, 21,159–21,173, doi:10.1029/1999JA000316.
- Frey, H. U., S. B. Mende, T. J. Immel, S. A. Fuselier, E. S. Clafin, J.-C. Gérard, and B. Hubert (2002), Proton aurora in the cusp, *J. Geophys. Res.*, *107*(A7), 1091, doi:10.1029/2001JA900161.
- Frey, H. U., S. B. Mende, S. A. Fuselier, T. J. Immel, N. Østgaard (2003), Proton aurora in the cusp during southward IMF, *J. Geophys. Res.*, *108*(A7), 1277, doi:10.1029/2003JA009861.
- Friis-Christensen, E., M. A. McHenry, C. R. Clauer, and S. Vennerstrøm (1988), Ionospheric travelling convection vortices observed near the polar cleft: A triggered response to sudden changes in the solar wind, *Geophys. Res. Lett.*, *15*, 253–256.
- Fuselier, S. A., S. P. Gary, M. F. Thomsen, E. S. Clafin, B. Hubert, B. R. Sandel, and T. Immel (2004), Generation of transient dayside subauroral proton precipitation, *J. Geophys. Res.*, *109*, A12227, doi:10.1029/2004JA010393.
- Haerendel, G. (1994), Acceleration from field-aligned potential drops, *Astrophys. J. Suppl. Ser.*, *90*, 765, doi:10.1086/191901.
- Haerendel, G. (2007), Auroral arcs as sites of magnetic stress release, *J. Geophys. Res.*, *112*, A09214, doi:10.1029/2007JA012378.
- Haerendel, G. (2009), Poleward arcs of the auroral oval during substorms and the inner edge of the plasma sheet, *J. Geophys. Res.*, *114*, A06214, doi:10.1029/2009JA014138.
- Haerendel, G. (2012), A tool for characterizing and evaluating Type II auroral arcs, *J. Geophys. Res.*, *117*, A06214, doi:10.1029/2012JA017523.
- Haerendel, G., and H. U. Frey (2014), Role and origin of the poleward Alfvénic arc, *J. Geophys. Res. Space Physics*, *119*, 2945–2962, doi:10.1002/2014JA019786.
- Hasegawa, H., M. Fujimoto, T.-D. Phan, H. Rème, A. Balogh, M. W. Dunlop, C. Hashimoto, and R. TanDokoro (2004), Transport of solar wind into Earth's magnetosphere through rolled-up Kelvin-Helmholtz vortices, *Nature*, *430*, 755–758, doi:10.1038/nature02799.
- Holmes, J. M., M. G. Johnsen, C. S. Deehr, X.-Y. Zhou, and D. A. Lorentzen (2014), Circumpolar ground-based optical measurements of proton and electron shock aurora, *J. Geophys. Res. Space Physics*, *119*, 3895–3914, doi:10.1002/2013JA019574.
- Hosokawa, K., S. E. Milan, M. Lester, A. Kadokura, N. Sato, and G. Björnsson (2013), Large flow shears around auroral beads at substorm onset, *Geophys. Res. Lett.*, *40*, 4987–4991, doi:10.1002/grl.50958.
- Hubert, B., J. C. Gérard, S. A. Fuselier, and S. B. Mende (2003), Observation of dayside subauroral proton flashes with the IMAGE-FUV imagers, *Geophys. Res. Lett.*, *30*(3), 1145, doi:10.1029/2002GL016464.
- Jin, Y., X.-Y. Zhou, J. Moen, and M. Hairston (2016), The auroral ionosphere TEC response to an interplanetary shock, *Geophys. Res. Lett.*, *43*, 1810–1818, doi:10.1002/2016GL067766.
- Kivelson, M. G., and D. J. Southwood (1991), Ionospheric traveling vortex generation by solar wind buffeting of the magnetosphere, *J. Geophys. Res.*, *96*, 1661–1667, doi:10.1029/90JA01805.
- Laundal, K. M., and N. Østgaard (2008), Persistent global proton aurora caused by high solar wind dynamic pressure, *J. Geophys. Res.*, *113*, A08231, doi:10.1029/2008JA013147.
- Liang, J., E. F. Donovan, G. J. Sofko, and T. Trondsen (2008), Substorm dynamics revealed by ground observations of two-dimensional auroral structures on 9 October 2000, *Ann. Geophys.*, *23*, 3599–3613, doi:10.5194/angeo-23-3599-2005.
- Liou, C.-C. Wu, R. P. Lepping, P. T. Newell, and C.-I. Meng (2002), Midday sub-auroral patches (MSPs) associated with interplanetary shocks, *Geophys. Res. Lett.*, *29*(16), 1771, doi:10.1029/2001GL014182.
- Lockwood, M., B. S. Lanchester, H. U. Frey, K. Throp, S. K. Morley, S. E. Milan, and M. Lester (2003), IMF control of cusp proton emission intensity and dayside convection: Implications for component and antiparallel reconnection, *Ann. Geophys.*, *21*, 955–982.
- Lopez, R. E. (2016), The integrated dayside merging rate is controlled primarily by the solar wind, *J. Geophys. Res. Space Physics*, *121*, 4435–4445, doi:10.1002/2016JA022556.
- Mende, S. B., et al. (2000), Far ultraviolet imaging from the IMAGE spacecraft: 3. Spectral imaging of Lyman alpha and OI 135.6 nm, *Space Sci. Rev.*, *91*, 287–318, doi:10.1023/A:1005292301251.
- Meurant, M., J.-C. Gérard, B. Hubert, V. Coumans, C. Blockx, N. Østgaard, S. B. Mende (2003), Dynamics of global scale electron and proton precipitation induced by a solar wind pressure pulse, *Geophys. Res. Lett.*, *30*(20), 2032, doi:10.1029/2003GL018017.
- Meurant, M., J.-C. Gérard, C. Blockx, B. Hubert, and V. Coumans (2004), Propagation of electron and proton shock-induced aurora and the role of the interplanetary magnetic field and solar wind, *J. Geophys. Res.*, *109*, A10210, doi:10.1029/2004JA010453.
- Milan, S. E., M. Lester, S. W. H. Cowley, and M. Brittacher (2000), Convection and auroral response to a southward turning of the IMF: Polar UVI, CUTLASS, and IMAGE signatures of transient magnetic flux transfer at the magnetopause, *J. Geophys. Res.*, *105*, 15,741–15,755, doi:10.1029/2000JA900022.
- Miura, A. (1992), Kelvin-Helmholtz instability at the magnetospheric boundary: Dependence on the magnetosheath sonic Mach number, *J. Geophys. Res.*, *97*, 10,655–10,675, doi:10.1029/92JA00791.
- Moen, J., D. A. Lorentzen, and F. Sigernes (1998), Dayside moving auroral forms and bursty proton auroral events in relation to particle boundaries observed by NOAA 12, *J. Geophys. Res.*, *103*, 14,855–14,863, doi:10.1029/97JA02877.
- Moen, J., H. C. Carlson, and P. E. Sandholt (1999), Continuous observation of cusp auroral dynamics in response to an IMF B_y polarity change, *Geophys. Res. Lett.*, *26*, 1243–1246, doi:10.1029/1999GL900224.
- Moen, J., J. A. Holtet, A. Pedersen, B. Lybekk, K. Svenen, K. Oksavik, W. F. Denig, E. Lucek, and M. André (2001), Cluster boundary-layer measurements and optical observations at magnetic conjugate sites, *Ann. Geophys.*, *18*, 1655–1668, doi:10.5194/angeo-19-1655-2001.
- Nakamura, T. K. M., D. Hayashi, M. Fujimoto, and I. Shinohara (2004), Decay of MHD-scale Kelvin-Helmholtz vortices mediated by parasitic electron dynamics, *Phys. Rev. Lett.*, *92*, 145001, doi:10.1103/PhysRevLett.92.145001.
- Newell, P. T., C.-I. Meng, D. G. Sibeck, and R. P. Lepping (1989), Some low altitude cusp dependencies on interplanetary magnetic field, *J. Geophys. Res.*, *94*, 8921–8927, doi:10.1029/JA094iA07p08921.
- Oieroset, M., P. E. Sandholt, W. F. Denig, and S. W. H. Cowley (1997), Northward interplanetary magnetic field cusp aurora and high-latitude magnetopause reconnection, *J. Geophys. Res.*, *102*, 11,349–11,362, doi:10.1029/97JA00559.
- Otto, A., and D. H. Fairfield (2000), Kelvin-Helmholtz instability at the magnetotail boundary: MHD simulation and comparison with Geotail observations, *J. Geophys. Res.*, *105*, 21,175–21,190, doi:10.1029/1999JA000312.

- Owen, C. J., M. G. G. T. Taylor, I. C. Krauklis, A. N. Fazakerley, M. W. Dunlop, and J. M. Bosqued (2004), Cluster observations of surface waves on the dawn flank magnetopause, *Ann. Geophys.*, *22*, 971–983, doi:10.5194/angeo-22-971-2004.
- Paschmann, G., W. Baumjohann, N. Sckopke, T.-D. Phan, and H. Lühr (1993), Structure of the dayside magnetopause for low magnetic shear, *J. Geophys. Res.*, *98*, 13,409–13,422, doi:10.1029/93JA00646.
- Paschmann, G., S. Haaland, B. U. Ö. Sonnerup, E. Georgescu, B. Klecker, A. Vaivads, H. Rème, T. D. Phan, and H. Hasegawa (2005), Characteristics of the near-tail dawn magnetopause and boundary layer, *Ann. Geophys.*, *23*(4), 1481–1497, doi:10.5194/angeo-23-1481-2005.
- Phan, T. D., and G. Paschmann (1996), Low-latitude dayside magnetopause boundary layer for high magnetic shear: 1. Structure and motion, *J. Geophys. Res.*, *101*, 7801–7815, doi:10.1029/95JA03752.
- Rae, I. J., et al. (2009), Near-Earth initiation of terrestrial substorm onset, *J. Geophys. Res.*, *114*, A00C09, doi:10.1029/2008JA013559.
- Rees, M. H., and D. Luckey (1974), Auroral electron energy derived from ratio of spectroscopic emissions 1. Model computations, *J. Geophys. Res.*, *79*, 5181–5186, doi:10.1029/JA079i034p05181.
- Rees, M. H., J. C. G. Walker, and A. Dalgarno (1967), Auroral excitation of the forbidden lines of atomic oxygen, *Planet. Space Sci.*, *15*, 1097–1110, doi:10.1016/0032-0633(67)90096-7.
- Russell, C. T. (2000), The polar cusp, in *Coordinated Measurements of Magnetospheric Processes*, *Adv. Space Res.*, *25*(7/8), 1413–1424.
- Russell, C. T. and M. Ginskey (1995), Sudden impulses at subauroral latitudes: response for northward interplanetary magnetic field, *J. Geophys. Res.*, *100*, 23,695–23,702.
- Sakaguchi, K., K. Shiokawa, A. Ieda, R. Nomura, A. Nakajima, M. Greffen, E. Donovan, I. R. Mann, H. Kim, and M. Lessard (2009), Fine structures and dynamics in auroral initial brightening at substorm onsets, *Ann. Geophys.*, *27*, 623–630, doi:10.5194/angeo-27-623-2009.
- Sandholt, P. E., C. J. Farrugia, M. Cqeroset, P. Stauning, and S. W. H. Cowley (1996), Auroral signature of lobe reconnection, *Geophys. Res. Lett.*, *23*, 1725–1728, doi:10.1029/96GL01846.
- Sandholt, P. E., C. J. Farrugia, M. Cqeroset, P. Stauning, and W. F. Denig (1998), Auroral activity associated with unsteady magnetospheric erosion: Observations on December 18, 1990, *J. Geophys. Res.*, *103*, 2309–2317, doi:10.1029/97JA01317.
- Shue, J.-H., J. K. Chao, H. C. Fu, C. T. Russell, P. Song, K. K. Khurana, and H. J. Singer (1997), A new functional form to study the solar wind control of the magnetopause size and shape, *J. Geophys. Res.*, *102*, 9497–9511, doi:10.1029/97JA00196.
- Sibeck, D. G., and G. I. Korotova (1996), Occurrence patterns for transient magnetic field signatures at high latitudes, *J. Geophys. Res.*, *101*, 13,413–13,428, doi:10.1029/96JA00187.
- Sibeck, D. G., W. Baumjohann, and R. E. Lopez (1989), Solar wind dynamic pressure variations and transient magnetospheric signatures, *Geophys. Res. Lett.*, *16*, 13–16, doi:10.1029/GL016i001p00013.
- Song, Y., and R. L. Lysak (1994), Alfvénon, driven reconnection and the direct generation of the field-aligned current, *Geophys. Res. Lett.*, *21*, 1755–1758.
- Sonnerup, B. U. Ö. (1980), Theory of the low-latitude boundary layer, *J. Geophys. Res.*, *85*, 2017–2026, doi:10.1029/JA085iA05p02017.
- Spann, J. F., M. Brittnacher, R. E. Elsen, G. A. Germany, and G. K. Parks (1998), Initial response and complex polar cap structures of the aurora in response to the January 10, 1997 magnetic cloud, *Geophys. Res. Lett.*, *25*, 2577–2580, doi:10.1029/98GL00647.
- Tamao, T. (1964), A hydromagnetic interpretation of geomagnetic SSC, *Rep. Ionos. Space Res. Jpn.*, *18*, 16.
- Torr, M. R., et al. (1995), A far ultraviolet imager for the international solar-terrestrial physics mission, *Space Sci. Rev.*, *71*, 329–383, doi:10.1007/BF00751335.
- Tsurutani, B. T., J. K. Arballo, G. S. Lakhina, C. Ho, B. Buti, J. S. Pickett, and D. A. Gurnett (1998), Plasma waves in the dayside polar cap boundary layer: Bipolar and monopolar electric pulses and whistler mode waves, *Geophys. Res. Lett.*, *25*, 4117–4120, doi:10.1029/1998GL900114.
- Tsurutani, B. T., X.-Y. Zhou, V. M. Vasyliunas, G. Haerendel, J. K. Arballo, and G. S. Lakhina (2001), Interplanetary shocks, magnetopause boundary layers and dayside auroras: The importance of a very small magnetospheric region, *Surv. Geophys.*, *22*(2), 101–130, doi:10.1023/A:1012952414384.
- Vorobjev, V. G., O. I. Yagodkina, D. G. Sibeck, K. Liou, and C.-I. Meng (2001), Polar UVI observations of dayside auroral transient events, *J. Geophys. Res.*, *106*, 28,897–28,911, doi:10.1029/2000JA000396.
- Young, R. A., and G. Black (1967), Deactivation of O (1D), *J. Chem. Phys.*, *47*, 2311–2318, doi:10.1063/1.1703312.
- Zhang, Y., L. J. Paxton, T. J. Immel, H. U. Frey, and S. B. Mende (2002), Sudden solar wind dynamic pressure enhancements and dayside detached auroras: IMAGE and DMSP observations, *J. Geophys. Res.*, *108*(A4), 8001, doi:10.1029/2002JA009355.
- Zhang, Y., L. J. Paxton, C.-I. Meng, D. Morrison, B. Wolven, H. Kil, and A. B. Christensen (2004), Double dayside detached auroras: TIMED/GUVI observations, *Geophys. Res. Lett.*, *31*, L10801, doi:10.1029/2003GL018949.
- Zhang, Y., L. J. Paxton, and Y. Zheng (2008), Interplanetary shock induced ring current auroras, *J. Geophys. Res.*, *113*, A01212, doi:10.1029/2007JA012554.
- Zhou, X. W., C. T. Russell, L. Guan, S. A. Fuselier, and J. D. Scudder (2000), Solar wind control of the polar cusp at high altitude, *J. Geophys. Res.*, *105*, 245–251, doi:10.1029/1999JA900412.
- Zhou, X.-Y., and E. J. Smith (2015), Super-criticality ICME and CIR shocks, *J. Geophys. Res. Space Physics*, *120*, 1526–1536, doi:10.1002/2014JA020700.
- Zhou, X.-Y., and B. T. Tsurutani (1999), Rapid intensification and propagation of the dayside aurora: Large scale interplanetary pressure pulses (fast shocks), *Geophys. Res. Lett.*, *26*, 1097–1100, doi:10.1029/1999GL900173.
- Zhou, X.-Y., R. J. Strangeway, P. C. Anderson, D. G. Sibeck, B. T. Tsurutani, G. Haerendel, H. U. Frey, and J. K. Arballo (2003), Shock-aurora: FAST and DMSP observations, *J. Geophys. Res.*, *108*(A4), 8019, doi:10.1029/2002JA009701.
- Zhou, X.-Y., K. Fukui, H. C. Carlson, J. I. Moen, and R. J. Strangeway (2009), Shock aurora: Ground-based imager observations, *J. Geophys. Res.*, *114*, A12216, doi:10.1029/2009JA014186.
- Zhou, X.-Y., D. G. Sibeck, O. Amm, and J. M. Ruohoniemi (2010), Interplanetary shock generated ionospheric traveling convection vortex near local noon, *Adv. Geosci.*, *21*, 367–378.